Fast Non-Empiric Tonal Noise Prediction Model for Installed Propulsors

Andrea Franco*
Cluster of Excellence SE²A –Sustainable and Energy-Efficient Aviation, Technische Universität Braunschweig, Germany
Institute of Aerodynamics and Flow Technology, Department of Technical Acoustics, German Aerospace Center (DLR), Lilienthalplatz 7, 38108 Braunschweig, Germany

Michael Mößner†, Roland Ewert‡, and Jan Werner Delfs§
Institute of Aerodynamics and Flow Technology, Department of Technical Acoustics, German Aerospace Center (DLR), Lilienthalplatz 7, 38108 Braunschweig, Germany

The increasing demand for cuts in environmental pollution is driving aircraft manufacturers towards sustainable aviation concepts that integrate unconventional propulsion configurations on the airframe. To aid the design process of new aircraft, a reliable prediction of installed rotor noise emissions would be required. Therefore, in this work an advanced rotor noise prediction approach is presented, which was developed to be fast and physical-principles-based, in order to be able to represent current and possibly newly arising noise sources mechanisms in complex configurations. The tool-chain proposed relies on aerodynamic predictions based on Actuator Disc (AD) Reynolds Averaged Navier Stokes (RANS) computations that provide the background flow solution for the Computational Aeroacoustics (CAA) method, which considers Gaussian regularised line-source distributions of strengths defined from either the obtained AD surface loads solution, or tabulated aerodynamic data used in combination with a model based on Blade Element Momentum Theory (BEMT). In this work initial successful results are reported for simplified test cases, outlining future possible applications.

I. Introduction

In the last decade, the increasing demand for international mobility has seen an equivalent growth in air transportation, therefore increasing its environmental impact. As a consequence, the necessary cuts in environmental pollution require sustainable aviation designs concepts that would need, among the targets to achieve, significant noise emission reductions. Sustainable approaches in aircraft design that include the integration of unconventional propulsion concepts on the airframe have been progressively proposed and adopted as viable solutions, therefore requiring reliable noise emissions' predictions tools to evaluate the feasibility of such proposals with regards to their environmental impact, directly aiding aircraft manufacturers during the design stage of an aircraft.

The state of the art of distributed propulsion concepts for sustainable aviation technologies includes fan engines configurations with Boundary Layer Ingestion (BLI), multi-propulsors involving in particular Contra Rotating Open Rotors (CROR) technologies, and wing-distributed engines arrangements with a focus on electrically driven propellers.

Electrically driven propellers are considered an interesting option in particular for reduced-size aircraft for regional transport and urban air mobility solutions. Although propeller noise sources have been extensively studied in past decades, future applications of this type of propulsion will require improved prediction capabilities for a reliable design that considers all realizable flow conditions. Approaches for noise estimation of propeller applications usually consider potential-flow-based aerodynamic predictions, such as the method reported in [1], where the implementation and results of a simplified method for propeller noise prediction based on the Ffowcs Williams and Hawkings (FWH) time domain solutions of Farassat are described. To produce the aerodynamic pressure data on the surface of the rotor blades, needed for the FWH-based calculations, simplified aerodynamic tools are considered to avoid a full CFD simulation. Steady blade loads are computed based on Blade Element Momentum Theories (BEMT), and flow non-uniformities are

*Research Scientist, Member AIAA, corresponding author: andrea.franco@dlr.de
†Senior Scientist
‡Senior Scientist, Senior Member AIAA
§Professor, Head of Dept. of Technical Acoustics, Senior Member AIAA

calculated as small unsteady perturbations to the steady load results, to account for the presence of near structures and their influence on noise propagation. The predicted aerodynamic performance indicators from the simplified tool-chain were found to be up to 10% lower than the CFD-predicted counterpart, but consistent with the simplifications introduced. In [2], two distributed electric propulsion configurations were investigated by comparing acoustics measurement data with the results of a tool-chain that included a lifting line solver combined with a free wake model for the blade steady aerodynamic loading, a FWH solver for the direct computation of the acoustics field, and a Boundary Element Method (BEM) solver for the propagation and scattering considering surrounding surfaces. Broadband noise was accounted for by the Amiet semi-analytical model. Promising results were reported regarding the validation of the method with the measured data, but computational inefficiencies were identified and would be addressed in future developments. More recent efforts included CFD prediction tools to account for viscous effects in the propeller slipstream, as introduced in [3], where the tool-chain used for the design of a flight demonstrator aircraft with distributed electric propulsion was described. The method introduced includes either a BEMT approach or a CFD based methodology for the aerodynamic predictions, and a FWH solver for the corresponding aeroacoustics calculations. The proposed approach was capable of capturing blade-passing-frequency effects of configurations involving flow conditions with different angles of attack, but the azimuthal influence on the noise response of the inflow conditions was seen to be captured only by the CFD based tool-chain, indicating as a possible improvement of the BEMT tool an increased azimuthal grid resolution.

Other simplified noise prediction options would consider reduced-order models, to allow an initial fast estimate of the benefits of the configuration investigated. In [4], a benchmark experiment was introduced, investigating pusher-propeller configurations that would include the ingestion of wakes such as the ones formed from pylons. Two bladed propellers were considered placed downstream of a NACA0015 blunt profile, and the measurements obtained included unsteady pressure data on the blade and far-field aeroacoustics data. A comparison of the measured data with a reduced-order approach was performed, which included blade loading predictions based on gust-response functions and FWH calculations for the acoustics sources. A promising accuracy of the numerical method adopted for comparison was reported, even though residual errors are highlighted for the loading calculations, and thickness noise contributions were not included.

The benefits of propeller applications are not necessarily limited to regional aircraft transportation, but can be applied for larger-sized aircraft through CROR technologies. CROR are a promising propeller-based solution for sustainable propulsion concepts with increased efficiency, for a range of Mach number flow conditions typical of conventional turbofan applications. Nevertheless, substantial noise emissions are produced, therefore requiring an appropriate installation solution for the aircraft concept to be defined. A possible solution is represented by hybrid-wing-body aircraft where the installed location of the CROR could be defined in order to maximize noise shielding by the airframe. In [5] results of an experimental campaign were reported with the aim of investigating noise shielding by a hybrid-wing-body aircraft with different open rotors configurations. This work was focused on the development of a future noise estimation method from the shielding data obtained. It was found that the tonal noise contributions from the front rotor, the aft rotor and from their interaction present different shielding characteristics, which are influenced by a variety of parameters including directivity, location of the distributed sources described by the rotors, and the incoherent features of the wake flows from the front rotor to the aft rotor. Due to the non-guaranteed amplitudes scalability in open rotors testing, it was proposed to study shielding effects for noise prediction modeling on the basis of three identified groups of tonal noise, namely front rotor, aft rotor and rotors-interaction tones.

Due to the costs associated with the realization and planning of experimental campaigns, often it is preferred to rely on numerical tools that could provide an indication for the most feasible applications. In [6] the results obtained from the development of a method for CROR noise prediction are described. The noise shielding effects of an installed rotors configuration were investigated close to different tail configurations. The method proposed includes acoustics predictions based on a FWH solver coupled with a BEM tool. The FWH tool was extended with the introduction of the Möhring's analogy so that the coupling velocity between the FWH solver and the BEM tool could be provided for cases with a low Mach number background mean flow. The integration surface of the Möhring analogy is based on flow variables obtained from Unsteady RANS (URANS) simulations. The approach introduced was reported to be capable of investigating the noise-shielding potential of the configurations analysed.

Other authors presented similar tool-chains based on coupled URANS-FWH methods, with comparable positive outcomes. In [7] an approach was presented based on results of a computational tool-chain including URANS simulations as a background mean flow for the acoustics prediction based on the FWH formulation 1A of Farassat. A clear distinction between noise sources' components in the Farassat formulation is assumed for the rotors configurations selected. Quadrupole and broadband noise sources were neglected. It was demonstrated that the method adopted could capture qualitatively the flow non-uniformities effects in the tonal noise predictions for the test cases selected.

Analogously, in [8] Stürmer compared the data from an experimental campaign of various CROR configurations with the results obtained from a tool-chain including URANS simulations and a FWH solver for the acoustics predictions. Good agreement between the simulated results and the measured data was highlighted, and differences between experiments and computations were attributed mainly to the lack of non-linearities prediction capabilities, as well as airframe reflection and refraction effects of the FWH permeable surface formulation.

Regarding unconventional fan engines applications, the preliminary prediction methods are required to capture a number of effects that would not be adequately represented by potential flow solutions, or reduced order models. Therefore, all proposed approaches rely on similar prediction capabilities that would include RANS or URANS simulations to obtain the necessary aerodynamic input for the acoustics prediction. The acoustics prediction tools used can be based on simplified theories or acoustics analogies, as described in [9], in which a full-scale turbofan engine was simulated to predict the inlet and aft noise propagation in installed conditions. The aerodynamics prediction was performed based on a URANS solver, while for the acoustics propagation either the Tyler-Sofrin rules for rotor noise in a duct or the Möhring's acoustics analogy were considered. Inlet noise was found to be mainly influenced by the inflow distortion, whereas aft noise was driven by the 2nd and 3rd blade-passing frequency predicted by the Tyler-Sofrin rules. In [10], the results obtained from a hybrid CFD-CAA approach were presented, where URANS results were coupled with the Möhring's analogy in predicting forward-radiated fan noise under disturbed inflow conditions. It was shown that inlet noise propagation for non-uniform inflow conditions can be correctly evaluated using a linear method. Another option for acoustics prediction approaches of fan BLI applications includes the use of FWH solvers, as described in [11], where the effects of inflow distortion for a BLI embedded propulsion system were investigated, focusing in particular on the turbulent flow developing over the fuselage at the fan inlet. In this work the aerodynamics features were resolved with a compressible Lattice Boltzmann solver, and a FWH solver was used for the acoustics predictions. From the configuration investigated, no clear tonal components could be identified in the sound response, while high broadband levels were detected. A different strategy for acoustics prediction of fan noise was documented in [12], in which the developments of a noise prediction solver aimed at predicting the acoustics radiation of a rear fan of a turbofan engine for a generic non-potential flow was introduced. The Linearized Euler Equations (LEE) were solved on a background RANS solution for the nearfield propagation, and the farfield response was computed with a FWH solver. The validation against measurements showed some discrepancies in the source levels, but overall the approach could predict the sound propagation for the industrial problem investigated.

Regardless of the specific applications considered, it is evident that all the previously mentioned novel sustainable propulsion technologies are currently investigated numerically by using either low-fidelity methods or fully-geometrically resolving approaches. No mid-fidelity approach that is capable, at a reduced computational cost, of considering all relevant aerodynamic effects for an accurate and fast acoustics solution is known to the authors to date. Following the recent developments included in [13], in which a fast and physical-principles-based rotor noise model was introduced, together with suitable adapted perturbation equations, in this work the rotor noise prediction method is expanded to consider realistic installed propulsion configurations. The proposed method, which is formulated to represent current and possibly newly arising noise sources mechanisms, is applied in a CAA framework in the time domain, and implemented in the unstructured quadrature-free experimental Discontinuous Galerkin (DG) CAA solver DISCO++ of DLR. The equations' system is solved on a tetrahedral grid, where, for each tetrahedron, the solution is represented with a third-order polynomial. Time integration is performed with a fourth-order Runge-Kutta method. Two options of the advanced rotor noise model are introduced, in combination with the proposed APE+VCE system of equations presented in [13], and validated with simplified test cases.

II. Rotor Source Noise Model Implementation

The rotor noise model is based on the approach introduced in [13], in which the rotor sources are modeled as three-dimensionally Gaussian regularised line-distributed input forces, rotating uniformly around the rotor axis. The line-distributed source values can be directly specified from BEMT input data, or indirectly from AD RANS solutions. Both options allow to solve for the perturbed variables on a background flow solution that includes the aerodynamic effect of a propulsor.

A. Model Based on Actuator Disc Surface Solution

For the model option based on the prescription of sources derived from an AD surface solution, the rotor load values obtained from the RANS solver are required to be prescribed on a two-dimensional circular surface, as exemplified in Fig. (1).

To define the appropriate source distributions from the AD RANS solution, the line sources are defined on the computational grid based on a local cylindrical coordinate system centered at the rotor hub being modeled. The line-distributed sources can be defined as straight or piecewise linear curves, at an initial location $\boldsymbol{X_{init}} = (r_{init}, \phi_{init}, x_{init})^T$ and with an initial strength at each radial location on the lines which reads as $w = \frac{1}{N_{blade}}$.

If the rotor being modeled consists of multiple blades N_{blade}, the initial location of each line-distributed source is determined assuming an equi-spaced circumferential offset $2\pi/N_{blade}$ applied to ϕ_{init}. Figure (2) shows the geometrical quantities of interest.

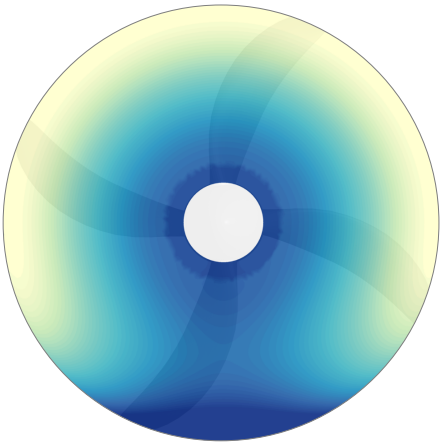

Fig. 1 Actuator disc RANS solution example.

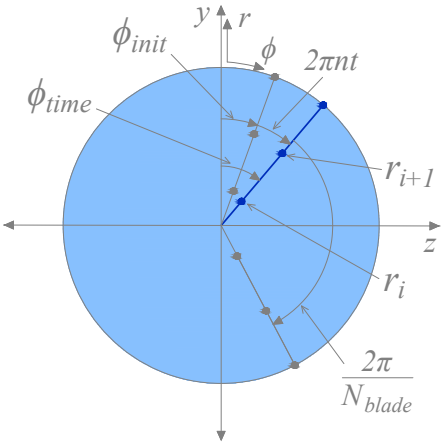

Fig. 2 Rotor cylindrical coordinate system for a line-distributed source.

The preliminary defined line-distributed sources are then regularised with a two step-procedure, based on the consideration that for straight or piecewise linear curves the radial preliminary source strength value is already known. In the first step the value at a given radial grid location r_{Grid} is obtained by linear interpolation of the initial strength value in the range $[r_i, r_{i+1}]$, resulting in $\boldsymbol{f_{Interp}} = (f_{Interp,r}, f_{Interp,\phi}, f_{Interp,x})^T$. The interpolation performed in the first step reduces the necessary dimensions over which regularising is required, so that in the second step the regularisation of the preliminary line sources is obtained by convolution of $\boldsymbol{f_{Interp}}$ with the Gaussian kernel $K(\phi_{Src}, x_{Src}, \phi_{Grid}, x_{Grid})$, defined as:

$$K(\phi_{Src}, x_{Src}, \phi_{Grid}, x_{Grid}) = \left(\frac{ln(2)}{\pi}\right) \frac{1}{\varepsilon^2} \exp\left(\frac{-ln(2) d_{LineSrc}^2}{\varepsilon^2}\right) / \mathrm{erf}\left(\frac{\pi\sqrt{(ln(2))} r_{Src}}{\varepsilon}\right) \tag{1}$$

in which

$$d = \sqrt{r_{Src}^2 (\phi_{Src} - \phi_{Grid})^2 + (x_{Src} - x_{Grid})^2} \tag{2}$$

is the distance measured on a cylindrical surface defined at a radius r_{Src}, where ϕ_{Src} is the line source azimuthal location, ϕ_{Grid} the grid point azimuthal coordinate, x_{Src} the line source axial location, and x_{Grid} the grid point axial coordinate. The variable ε represents the half-width at half-maximum of the Gaussian kernel. The Gaussian kernel $K(\phi_{Src}, x_{Src}, \phi_{Grid}, x_{Grid})$ is derived from a 2D Gaussian Kernel independent of the r coordinate, and averaged with an integration over the circumference, so that the resulting projected source, if integrated over the computational domain, would correspond to a unitary strength value. The error function term erf appearing at the denominator $K(\phi_{Src}, x_{Src}, \phi_{Grid}, x_{Grid})$ results from the integration, and for a given radius r_{Src} represents a constant scale factor. Figure (3), Fig. (4), and Fig. (5) show a possible definition of line sources from a given rotor blades geometry, and its corresponding line source regularisation with the procedure described.

The regularised source values obtained from Eq. (1) are described as the sum of a steady mean and a fluctuating component, where only the fluctuating component is of interest for the system of perturbation equations considered. Hence, the perturbed regularised force values are calculated as $\boldsymbol{S'} = \boldsymbol{S} - \boldsymbol{S_{mean}}$, where the mean value $\boldsymbol{S_{mean}}$ is computed as the average source value over a rotor revolution, which in the case of constant rotational speed can be alternatively expressed as a spatial integral over a ring of given radius. After the regularisation of the preliminary

sources of constant strength w, the related fluctuating sources' values $\boldsymbol{S'}$ are multiplicated with the load values on the AD surface, which is obtained through a Lagrangian high-order interpolator at a given radial and azimuthal coordinate on the circular surface. Figure (6) illustrates a possible line source distribution definition. The result of the multiplication is in the end scaled by the local circumference for a given radius, and assigned to the appropriate point of the DG discretization. The described procedure ensures that the integrated line-distributed sources values correspond to the original load values on the AD surface, and it is applied at each time dependent source location identified by the circumferential coordinate ϕ_{time}, updated according to the sources revolutions per second n prescribed in input.

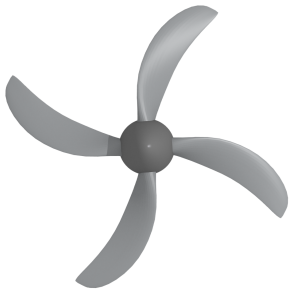

Fig. 3 Original rotor blades to be modeled.

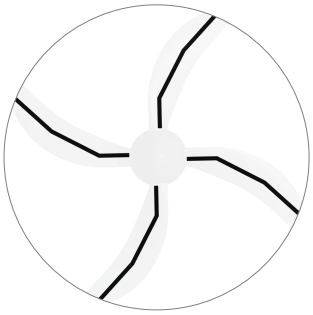

Fig. 4 Line sources of constant strength w, defined from the original rotor blades.

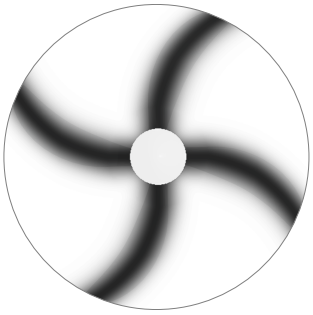

Fig. 5 Regularisation of line sources of strength w.

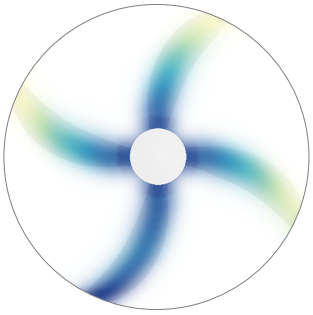

Fig. 6 Rotor sources from multiplication of interpolated AD sources with the line distributed sources of preliminary strength.

B. Model Based on Blade Element Momentum Theory

The option included in the model that allows to prescribe noise sources from BEMT differs from the model described in Sec. (II.A) in the source values definition, but maintains the overall approach regarding the regularisation of line sources. The definition of the line-distributed sources is based on a local cylindrical coordinate system centered at the rotor hub being modeled, with sources that can be defined as straight or piecewise linear curves, at an initial location $\boldsymbol{X_{init}} = (r_{init}, \phi_{init}, x_{init})^T$. If multiple blades N_{blade} are considered, the initial location of each line-distributed source is determined assuming an equi-spaced circumferential offset $2\pi/N_{blade}$ applied to ϕ_{init}. Figure (2) is the reference for the geometrical quantities of interest. The source values to be regularised are based on the local sectional lift L and sectional drag D of the blade airfoil sections, determined from the flow kinematics in the sectional plane shown in Fig. (7), where L and D are defined in the aerodynamic coordinate system which is obtained by rotating the $-x$ and $-Azim$ axis by the angle ϕ of the vector of the inflow velocity q at the airfoil.

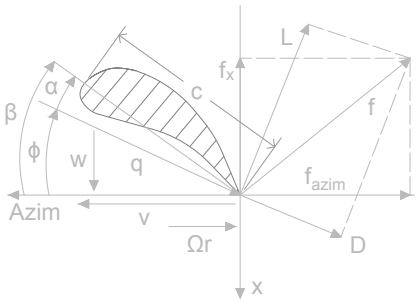

Fig. 7 Flow kinematics reference for the BEMT-based model.

The angle of attack α of the chord relative to q is obtained as:

$$\alpha = \beta - \phi \tag{3}$$

in which β is the twist angle of the chord relative to the propeller plane. The angle ϕ and the inflow velocity q depend on the rotational speed Ωr and the flow velocity of components (w, v) in the local coordinate system $(x, Azim)$ of the sectional plane, and are obtained as:

$$\phi = atan2(\frac{w}{\text{sgn}(\Omega)(\Omega r - v)}) \tag{4}$$

and

$$q = \sqrt{w^2 + (\Omega r - v)^2} \tag{5}$$

The local flow velocity is defined as the sum of the local mean flow and fluctuating velocity vector $(w, v) = (w_0, v_0) + (w', v')$, where $(w', v') = (w^a + w^r, v^a + v^r)$ is defined as the sum of the acoustic and hydrodynamic perturbed velocity vector defined in Sec. (III), to account for sound generation due to local flow disturbances.

For the sectional lift L and sectional drag D calculation, the necessary quantities are determined from tabulated values of airfoil chord length c, twist angle β, lift coefficient characteristic $c_L(\alpha)$ and drag coefficient characteristic $c_D(\alpha)$ for different blade sections. Lift coefficient and drag coefficient characteristics are tipically obtained from 2D CFD simulations of the corresponding sectional blade airfoil profiles. For intermediate angles of attack α and blade radial sections locations r, the values of $c_L(\alpha)$ and $c_D(\alpha)$ are obtained performing bilinear interpolation of the tabulated values at the specified r and α, whereas values of chord c and twist angle β at the specified r location are linearly interpolated from the tabulated values prescribed in input.

If the local angle of attack computed with Eq. (3) exceeds the limits of the values defined in the input table for a given radial location, the values of $c_L(\alpha)$ and $c_D(\alpha)$ are computed with a constant extrapolation of either the corresponding maximum or minimum aerodynamic coefficient value at the radial location considered. The lift L and drag D are then calculated from the interpolated values of $c(r)$, $\beta(r)$, $c_L(\alpha)$, $c_D(\alpha)$ as:

$$L = \frac{\rho}{2} q^2 c(r) c_L(\alpha) \tag{6}$$

$$D = \frac{\rho}{2} q^2 c(r) c_D(\alpha) \tag{7}$$

where ρ denotes the density of the medium. To determine the source values to be regularised, in a first step the axial component f_X and the azimuthal component f_{Azim} of the resulting sectional load f are computed as:

$$f_X = -Lcos(\phi) + Dsin(\phi) \tag{8}$$

$$f_{Azim} = \text{sgn}(\Omega)(Lsin(\phi) + Dcos(\phi)) \tag{9}$$

The sources to be prescribed in the rotor noise simulations need to be determined from the forces acting on the medium, therefore the final source values are determined as the opposite of the f_X and f_{Azim} values computed from Eq. (8) and Eq. (9) respectively. The source vector to be regularised is defined as $\boldsymbol{S} = (S_r, S_{Azim}, S_X) = (0, -f_{Azim}, -f_X)$.

The line-distributed sources are obtained with the same two step-procedure described in Sec. (II.A), considering Eq. (1) and Eq. (2) for the regularisation of $\boldsymbol{S}$. After the regularisation step, the fluctuating source values $\boldsymbol{S'}$ are determined as $\boldsymbol{S'} = \boldsymbol{S} - \boldsymbol{S_{mean}}$, where $\boldsymbol{S_{mean}}$ is defined as the average source value over a rotor revolution and computed as in Sec. (II.A), considering that for a constant rotational speed, $\boldsymbol{S_{mean}}$ can be alternatively expressed as a spatial integral over a ring of given radius. The source value to be averaged for determining $\boldsymbol{S_{mean}}$ is calculated based on the local load components obtained from Eq. (8) and Eq. (9), with the local mean flow velocity vector (w_0, v_0).

The described procedure is applied at each time dependent source location identified by the circumferential coordinate ϕ_{time}, updated according to the sources revolutions per second n prescribed in input.

C. Thickness Noise Source Calculation

In addition to the prescription of regularised line-distributed loads, the rotor noise model includes the option of defining thickness noise sources for both the modeling options described in Sec. (II.A) and Sec. (II.B).

To prescribe thickness noise sources, the distribution of mass of medium displaced by the propeller blade is defined as $m(r_{Src}) = A_{airfoil}(r_{Src})\rho$, where $A_{airfoil}(r_{Src})$ is the area of the blade sectional airfoil profile at a given radial location along the blade span. In order to prescribe thickness noise source contributions, the calculation of the time derivative of the mass distribution $\dot{m}(r_{Src})$ has to be computed, which for a regularised source reads as:

$$\dot{m}_{Regularised}(r_{Src}) = \frac{\partial(m_{Regularised}(r_{Src}))}{\partial t} = \frac{\partial(m(r_{Src}) \cdot K(\phi_{Src}, x_{Src}, \phi_{Grid}, x_{Grid}))}{\partial t} \tag{10}$$

in which $K(\phi_{Src}, x_{Src}, \phi_{Grid}, x_{Grid})$ is the Gaussian kernel introduced in Eq. (1). Assuming a constant mass distribution $m(r_{Src})$, the calculation of the source $\dot{m}_{Regularised}(r_{Src})$ in Eq. (10) can be simplified further obtaining:

$$\dot{m}_{Regularised}(r_{Src}) = \frac{\partial(m(r_{Src}) \cdot K(\phi_{Src}, x_{Src}, \phi_{Grid}, x_{Grid}))}{\partial t} = \tag{11}$$
$$m(r_{Src}) \cdot \frac{\partial(K(\phi_{Src}, x_{Src}, \phi_{Grid}, x_{Grid}))}{\partial t} = m(r_{Src}) \cdot \frac{\partial(K(\phi_{Src}, x_{Src}, \phi_{Grid}, x_{Grid}))}{\partial \phi} \frac{\partial \phi}{\partial t}$$

The time derivative $\frac{\partial \phi}{\partial t}$ is the angular speed $\Omega = 2\pi n$ of the rotor. Since the Gaussian kernel $K(\phi_{Src}, x_{Src}, \phi_{Grid}, x_{Grid})$ has the property of zero mean for its angular derivative $\frac{\partial(K(\phi_{Src}, x_{Src}, \phi_{Grid}, x_{Grid}))}{\partial \phi}$, it can be obtained that $\dot{m}_{Regularised}(r_{Src}) = \dot{m'}_{Regularised}(r_{Src})$, and after computing the derivatives in Eq. (11) the regularised thickness source definition reads as:

$$\dot{m'}_{Regularised}(r_{Src}) = m(r_{Src}) \frac{\Delta\phi \cdot r_{Src}^2 \cdot \frac{2}{\varepsilon^4} \frac{(\ln(2))^2}{\pi} \cdot \exp\left(-\ln(2) \cdot \left(\frac{d}{\varepsilon}\right)^2\right)}{\operatorname{erf}\left(\pi \cdot \sqrt{\ln 2} \cdot \frac{r_{Src}}{\varepsilon}\right)} \Omega \tag{12}$$

with the angle difference $\Delta\phi = (\phi_{Src} - \phi_{Grid}) + n \cdot 2\pi$, normalized to have an angle in the range $[-\pi, \pi]$.

The distribution of mass of medium can be either prescribed on a circular surface, according to the source noise model described in Sec. (II.A), or it can be specified as an additional generic line source in addition to the load sources defined by the model option of Sec. (II.B). If the model option in Sec. (II.A) is considered, the thickness noise source value needs to be scaled by the local circumference for a given radius.

The resulting thickness noise source value obtained from Eq. (12) is the fluctuating thickness noise source $\dot{\theta}'$ to be assigned to the appropriate point of the DG discretization.

III. APE+VCE System Of Perturbation Equations

In a previous work [13], a newly defined system of equations was presented for robust computations of applications including complex geometries where an adequate description of the interaction of acoustic and vortical eigenmodes would be required.

The system of equations was derived from the LEE in their primitive variables formulation, on the assumption that isentropic flow conditions would be representative of future possible applications of the model.

The perturbed velocities $\boldsymbol{u'}$ of the isentropic LEE are decomposed in a potential (acoustic) component and a non-acoustic component, resulting in the system of equations which reads as:

$$\frac{\partial p'}{\partial t} + c_0^2 \nabla \cdot \left(\boldsymbol{u_0} \frac{p'}{c_0^2} + \rho_0 \boldsymbol{u^a} \right) = -c_0^2 \nabla \cdot (\rho_0 \boldsymbol{u^r}) + c_0^2 \dot{\theta}' \tag{13}$$

$$\frac{\partial \boldsymbol{u^a}}{\partial t} + \nabla(\boldsymbol{u^a} \cdot \boldsymbol{u_0}) + \nabla \left(\frac{p'}{\rho_0} \right) = \boldsymbol{0} \tag{14}$$

$$\frac{\partial (\rho_0 \boldsymbol{u^r})}{\partial t} + \nabla \cdot (\rho_0 \boldsymbol{u_0} \boldsymbol{u^r}) + \rho_0 (\boldsymbol{u^r} \cdot \nabla) \boldsymbol{u_0} = -\rho_0 \boldsymbol{\omega_0} \times \boldsymbol{u^a} + \boldsymbol{f'} \tag{15}$$

In the equations, ρ, $\boldsymbol{u}$, p, and t are the density, velocity, pressure, and time, respectively, with subscript 0 indicating mean flow quantities and primed symbols indicating perturbation quantities. Both the speed of sound c_0 and the vorticity vector $\boldsymbol{\omega_0}$ are computed from the mean flow. $\boldsymbol{u^a}$ describes the potential (acoustic) component of the perturbed velocity of the LEE, while $\boldsymbol{u^r}$ is the non-acoustic component of the LEE velocity, which includes the solenoidal field of the LEE. $\dot{\theta}'$ represents air displacement type of sources, and $\boldsymbol{f'}$ externally prescribed fluctuating forces of the LEE. Further details on the intermediate steps of the equations' system derivation are included in [13].

To realize a robust method, the term $+\rho_0(\boldsymbol{u^r} \cdot \nabla)\boldsymbol{u_0}$, corresponding to the source of hydrodynamic instabilities, is neglected, as well as the term $-\rho_0 \boldsymbol{\omega_0} \times \boldsymbol{u^a}$, which would represent a feedback from the acoustics to the entropy mode and can be considered not relevant for the installed applications configurations of interest. The resulting Vortical Convection Equation (VCE), Eq. (15), is a convection equation for the variable $\rho_0 \boldsymbol{u^r}$ and could still present numerical instabilities for certain background mean flow definitions. To further stabilize the VCE equation, numerical limiting techniques can be applied. The results included in this work adopt a limiter derived from maximum-principle-satisfying formulations, which limits $\rho_0 \boldsymbol{u^r}$ within the maximum and minimum initial solution values. The boundary conditions implemented are based on an upwind flux vector splitting approach. On the domain outer surfaces, a non-reflecting boundary condition is applied, with prescribed null incoming eigenmodes. The wall boundary condition used is based on a ghost point approach, where an additional ghost point with identical coordinates as the high order points on a tetrahedral face describing the wall surface is added. At the wall surfaces, the inner tetrahedral flux cell state is prescribed based on the interior solution, and the ghost point cell state has a slip-wall velocity definition for the potential components $\boldsymbol{u^a}$, and a null prescribed incoming eigenmodes definition for the non-acoustic component $\boldsymbol{u^r}$.

IV. Validation

The predictions capabilities of the proposed advanced rotor noise model in combination with the APE+VCE equations' system are verified with a test case based on the Agard propeller E6 test case [14]. The relevant data for the simulations are included in Table (1).

Table 1 Agard E6 test case input parameters

Input Parameter	Value
Free-stream Mach nr. M_∞	0.15
n	110.83 s^{-1}
Propeller Blade Length R	0.32 m
Number Of Blades N_{Blade}	4
Blade Tip Mach nr. M_{tip}	0.65

Comparisons of the sound generation for an isolated configuration and for an installed configuration are presented, to highlight the model capability of predicting the related installation effects. For the installed configuration, the DU-96-W-180 airfoil profile was considered, with a chord length of $1.87R$. The CFD RANS AD simulations are based on the model presented in [15], implemented in the DLR TAU code [16]. The computational grids generated for the CFD simulation are hybrid, including hexahedra in regions where viscous flow effects are to be captured, and pyramids and tetrahedra for regions away from viscous walls. Nacelle, spinner and wing profile are assigned a turbulent viscous wall boundary condition, and the actuator disc surfaces the related boundary condition. Remaining surfaces are assigned a farfield boundary condition.

The turbulence model selected is the SA model [17]. Figure (8) illustrates the computational domain for the RANS simulations of the isolated configuration. The domain definition of the RANS simulations of the installed configurations is instead shown in Fig. (9). The TAU AD model requires lift and drag coefficient characteristics of the rotor blades to simulate, together with the related blade chord and twist angle distributions. Figure (10) and Fig. (11) illustrate the lift and drag coefficient curves respectively, obtained from the data included in [15] for nine different blade sections. The related chord and twist distributions are included in Fig. (12). Figure (13) shows the blade sectional area distribution, used for the thickness noise source definition.

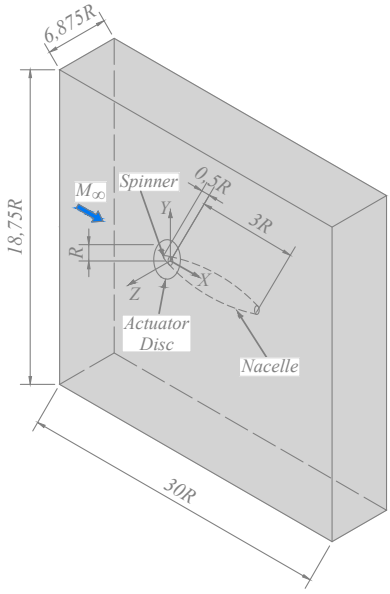

Fig. 8 RANS computational domain for the isolated case.

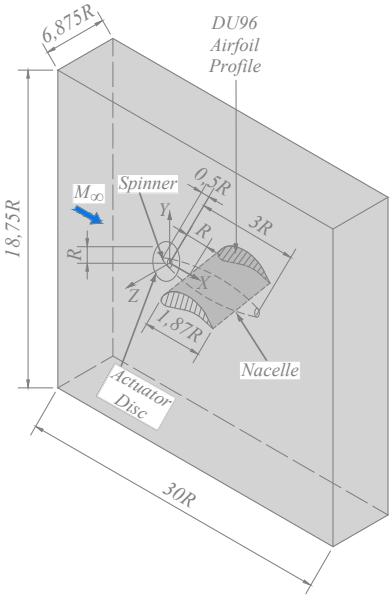

Fig. 9 RANS computational domain for the installed case.

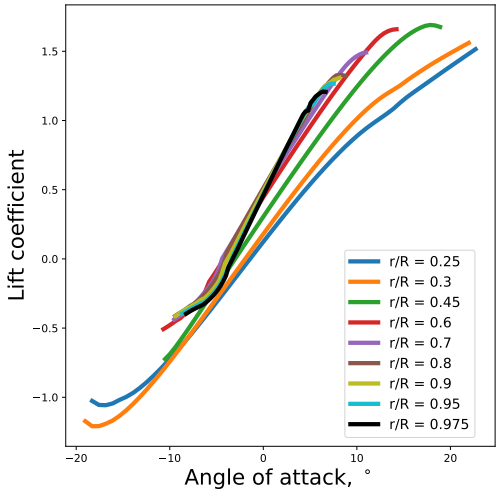

Fig. 10 Lift coefficient characteristic for the selected blade sections.

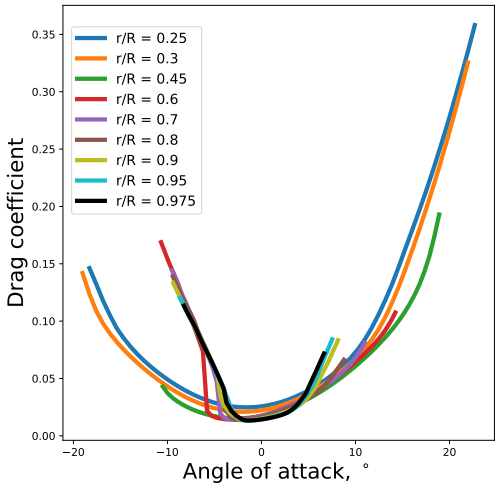

Fig. 11 Drag coefficient characteristic for the selected blade sections.

As for the CAA simulations, the computational domains realized are similar to the domains for the CFD calculations, without the AD surface prescription and including a cylindrical refinement region to appropriately resolve the propagating tip vortices. Figure (14) illustrates the computational domain for the CAA simulations of the isolated configuration. The domain definition of the CAA simulations of the installed configurations is instead shown in Fig. (15).

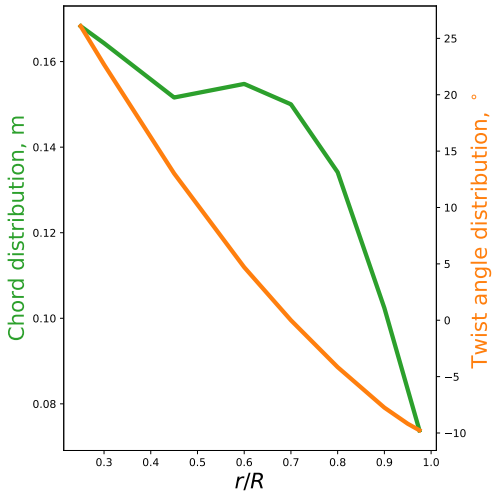

Fig. 12 Chord and twist angle distributions for a single blade.

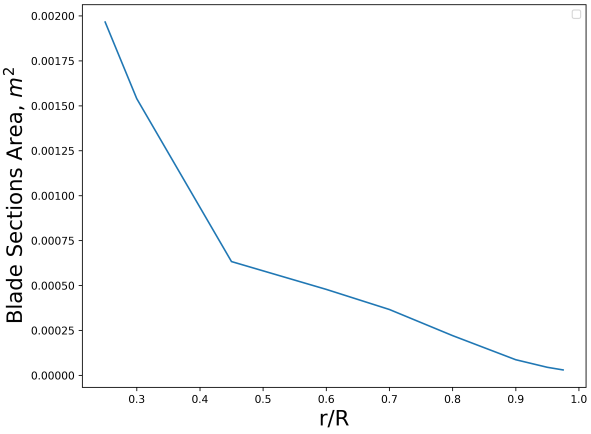

Fig. 13 Blade sections area for a single blade.

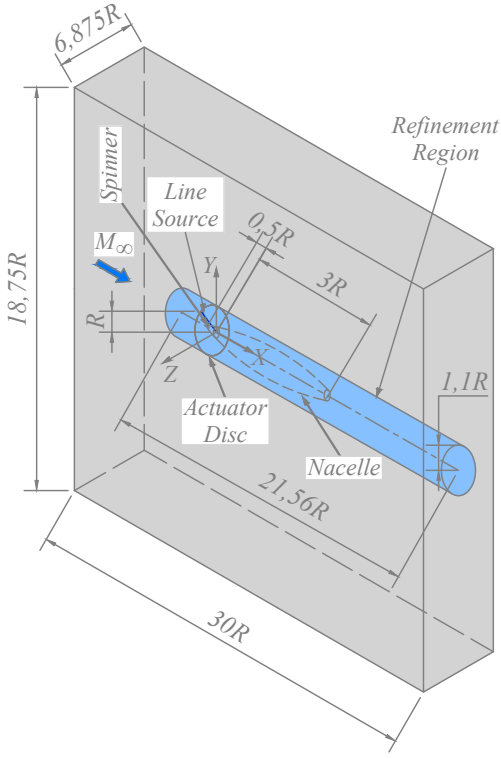

Fig. 14 CAA computational domain for the isolated case.

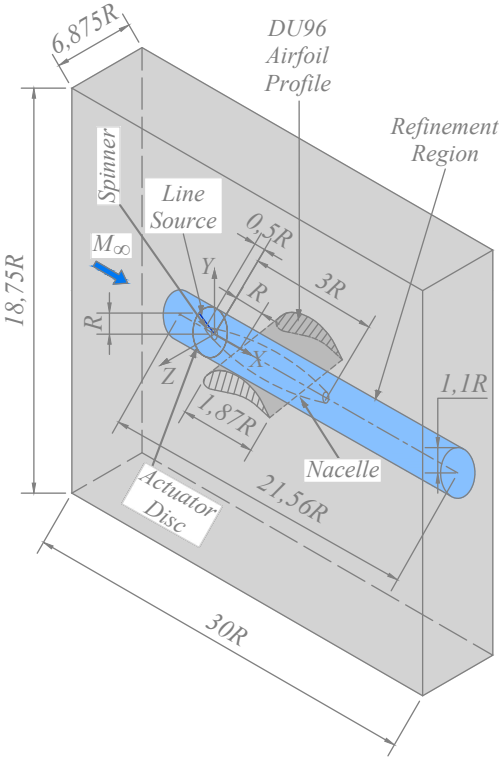

Fig. 15 CAA computational domain for the installed case.

The rotating straight line sources are defined in the y-z plane centered at the origin of the coordinate system, which corresponds to the AD location of the CFD simulations. No AD geometrical surface definition is required for CAA simulations. In the farfield, the size of the tetrahedral cells is specified to resolve the first three harmonics, and in the refinement region it is reduced to 1/10 of the farfield tetrahedral edge length. A ratio of $\varepsilon/\Delta x_{Ref} = 2$ was selected for the Gaussian regularized sources. The nacelle, spinner and wing profile are assigned the wall boundary condition described in Sec. (III), while all the remaining boundaries are assigned a boundary condition of the non-reflecting type, with the same formulation as explained in Sec. (III). Approximately five complete revolutions of the line source are simulated. Table (2) summarises the CAA simulations input parameters.

Table 2 CAA simulations input parameters

Input Parameter	Value
Free-stream Mach nr. M_∞	0.15
n	110.83 s^{-1}
Propeller Blade Length R	0.32 m
Farf. Tetra Cell Size Δx_{Far}	0.6813
Refin. Tetra Cell Size Δx_{Ref}	0.06813
Number of Time Steps	80, 000
Time Step Size	0.0007

An initial inspection of the results shows that the acoustics prediction method can capture qualitatively the expected phenomena. The CAA results based on the background flow solution provided by the corresponding AD RANS simulations are shown in Fig. (16), Fig. (17), Fig. (18), and Fig. (19), where the contours of the pressure fluctuations are shown with the Q-Criterion iso-surfaces superimposed, which describe the convected tip vortices. The comparison of the AD-based model results between the installed and isolated configuration of Fig. (16) and Fig. (17) shows small pressure fluctuations in the slipstream flow region, which correspond to the area in the vicinity of the convecting vortices. Close to the propeller, sound is propagated mainly in the radial direction, influenced by the predominant interaction of the tip vortices with the leading edge of the wing profile, and in the vicinity of the spinner of the propeller scattered pressure perturbations are identifiable. The results obtained from the BEMT-based model, included in Fig. (18), and Fig. (19) show a stronger acoustic response in the vicinity of the propeller, which could be attributable to the additional contribution of the velocity fluctuations increasing the source computed value. The influence of the perturbed velocities is not considered in the AD-based model due to its definition. More uniform contour levels are detectable, which could be caused by the local perturbed velocity influence in the source computation, decreasing the sound generation due to the scattered vorticity caused by the tip vortices. All the subsequent results are presented in terms of Sound Pressure Level (SPL). The energy content of the solution is described considering the 1st, 2nd, and 3rd harmonic of the fluctuating pressure signals, captured on planes centered at the propeller with virtual microphones, placed at a distance of 4R from the origin of the propeller's cylindrical coordinate system. The pressure signals are captured on the x-y coordinates plane. In Fig. (20) the directivity pattern in terms of SPL of the generated sound is compared for the isolated and installed configuration results produced by the AD-based model. A clear distinction between the installed and isolated test cases is identifiable for all the harmonics investigated. An increase in SPL is seen between 135° and 225°, which would correspond to the sound generated due to the tip vortices interaction with the wing leading edge. For the region between −30° and 30°, no major differences are detectable in SPL, with a slight decrease in SPL for the installed configuration. Higher harmonics show increasingly complex patterns. The implementation of the AD-based model allows to consider separately the effect of different load distributions for a given background mean flow. This feature is used in investigating the capabilities of the advanced rotor model in predicting both source and acoustic installation effects. In Fig. (21) the AD surface solutions of the previously computed installed and isolated configurations are considered for the same background RANS mean flow of the installed configuration, showing that the sound response of the two different load distribution for the examined flow configuration is almost identical when investigating the 1st harmonic, while clear differences are seen for the 2nd and 3rd harmonics, with higher SPL due to the AD surface loads of the installed configuration. The source installation effects detectable in this particular case are present only for the higher harmonics.

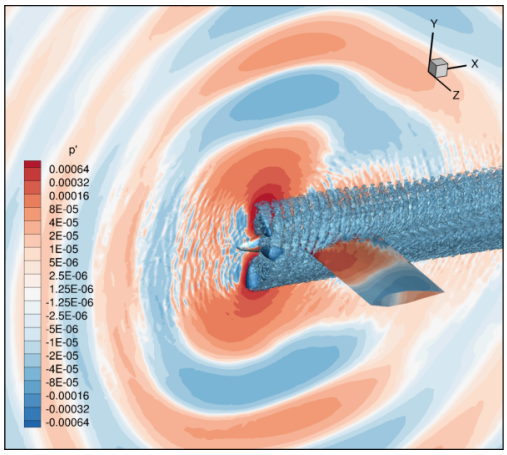

Fig. 16 Contour plot of p' for the installed propeller configuration, with Q-Criterion superimposed. Results obtained from the AD-based model.

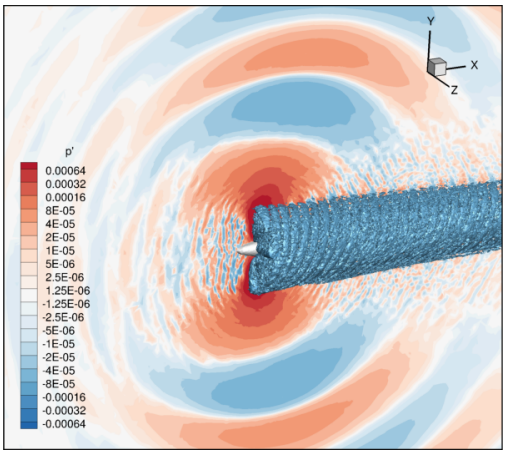

Fig. 17 Contour plot of p' for the isolated propeller configuration, with Q-Criterion superimposed. Results obtained from the AD-based model.

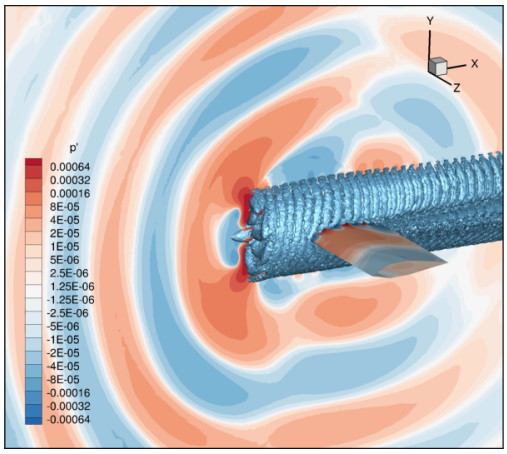

Fig. 18 Contour plot of p' for the installed propeller configuration, with Q-Criterion superimposed. Results obtained from the BEMT-based model.

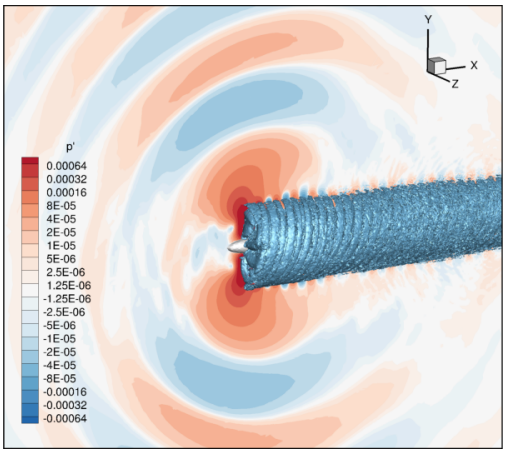

Fig. 19 Contour plot of p' for the isolated propeller configuration, with Q-Criterion superimposed. Results obtained from the BEMT-based model.

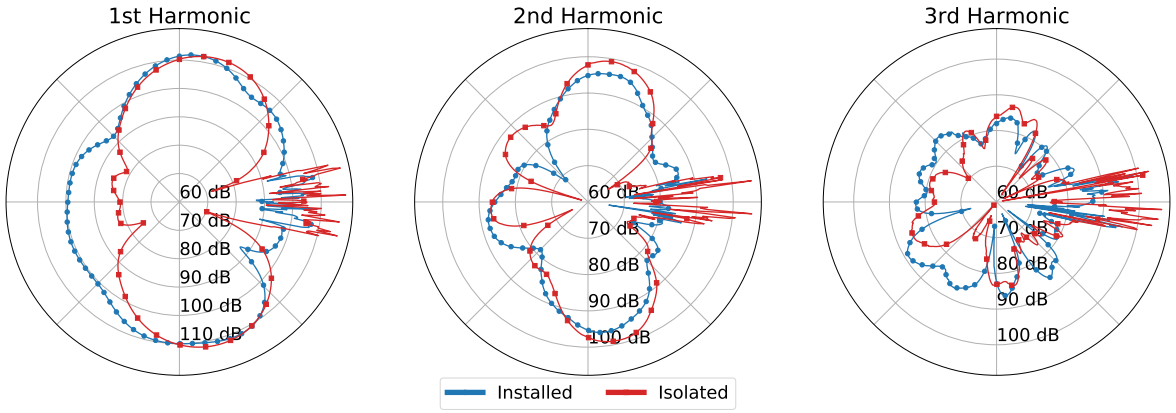

Fig. 20 SPL (dB) for the installed and isolated configurations, at a distance of 4R from the propeller.

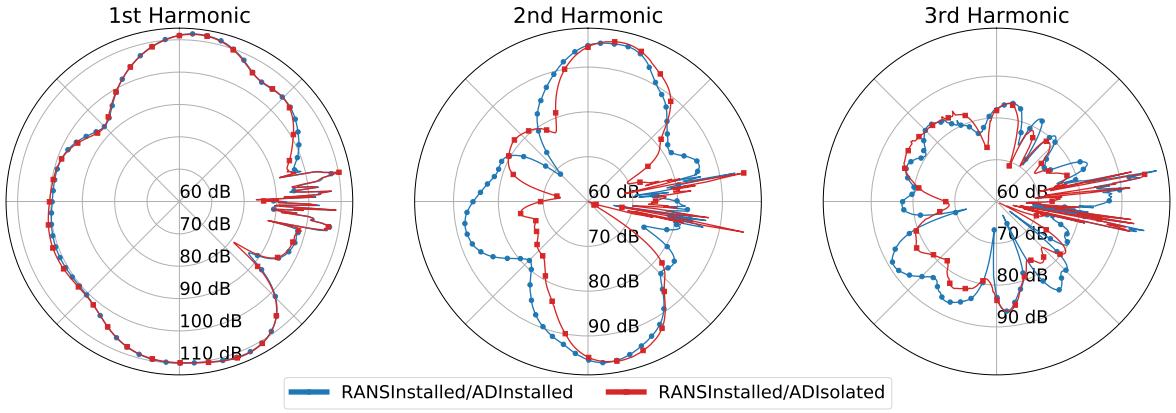

Fig. 21 SPL (dB) for different AD surface solutions and same RANS mean flow of the installed configuration, at a distance of 4R from the propeller.

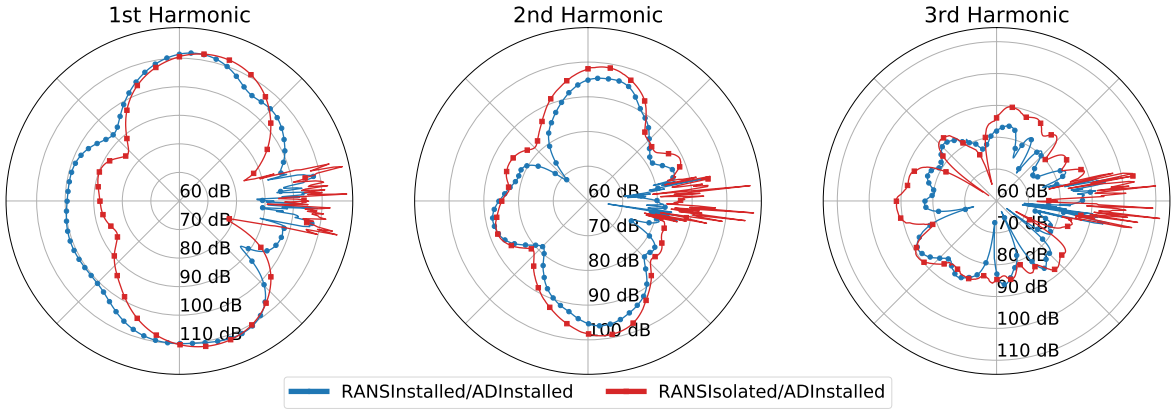

Fig. 22 SPL (dB) for different RANS mean flow and same AD surface solution of the installed configuration, at a distance of 4R from the propeller.

In Fig. (22) the same loads distribution of the installed configuration is considered for the background RANS solutions obtained for the isolated and installed configuration. In this case the influence on the sound response due to the presence of the wing profile is clearly captured by the model, indicating how the SPL difference seen for the 1st harmonic in Fig. (20) are mainly an acoustic installation effect. Higher harmonics show less differences in SPL amplitudes, with similar patterns.

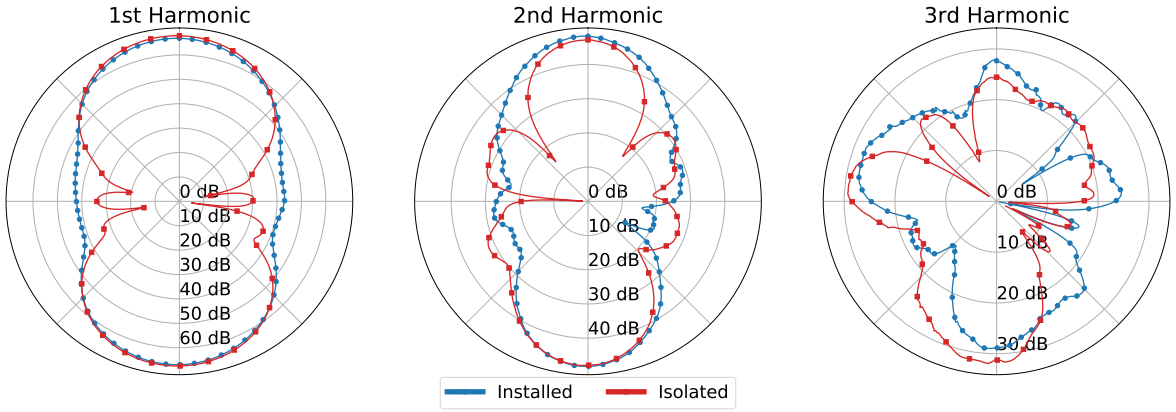

Fig. 23 SPL (dB) of the thickness noise source for the installed and isolated configuration, at a distance of 4R from the propeller.

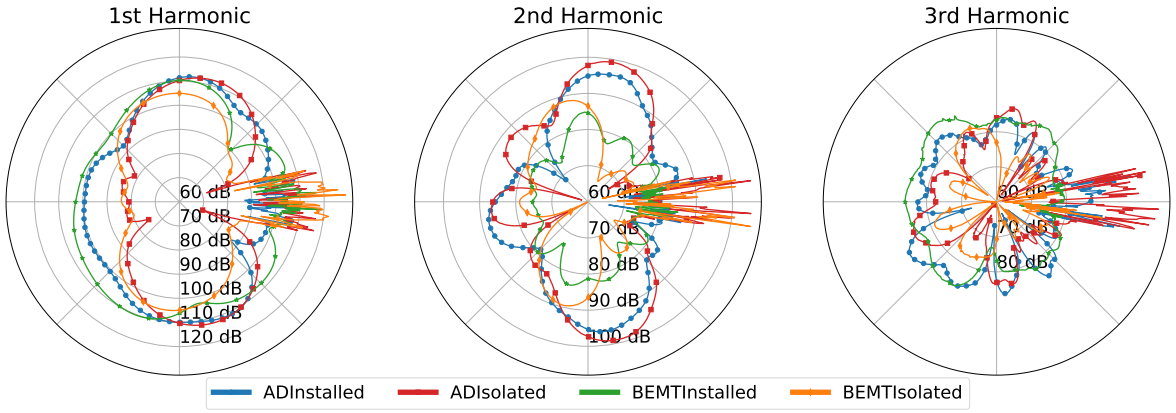

Fig. 24 SPL (dB) comparison of the installed and isolated configuration for solutions produced by AD-based and BEMT-based model, at a distance of 4R from the propeller.

Figure (23) shows the comparison of the effects of the thickness noise source for the installed and isolated configuration. Different directivity patterns are detected for the two configurations investigated, which indicate an acoustic installation effect. The overall SPL amplitudes are similar for the 1st and 2nd harmonic, while the 3rd harmonic shows considerably low levels, with a different directivity which is probably highly influenced by roundoff/approximation errors in the solution. Overall, the thickness noise source predictions are consistent with the expected low levels for the propeller operating conditions considered. As a last comparison, the results produced by the AD-based and the BEMT-based models are shown in Fig. (24) for the installed and isolated configuration. For the comparison of the results of the installed configuration by the two rotor model options, it can be seen that the BEMT-based model predicts values close to the AD-based model for the 1st harmonic, but of higher amplitudes in the plot region between 135° and 225°, caused by the additional source contributions from the perturbed velocities. The SPL values downstream of the wing are almost not affected by the the different model chosen. For the 2nd harmonic, considerably lower levels are detected by the BEMT-based model, which could be caused by source contributions by the fluctuating velocities canceling out contributions from the mean flow. For the isolated configuration, lower levels are noticed for the BEMT-based predictions. The comparison of the results of the BEMT-based and AD-based model shows how the BEMT-based model can produce significantly different levels when non-negligible velocity fluctuations are present in the solution.

V. Conclusion

An advanced CAA method for the prediction of the sound generated from installed rotors was developed, based on AD RANS simulations that would provide the background flow solution for the acoustics approach proposed. The CAA method includes regularised line-distributed sources of strength derived from the AD surface loads obtained from the RANS calculation, or line sources prescribed based on BEMT. The rotor noise source model proposed is applied in combination with the newly proposed APE+VCE system of perturbation equations. The aim of the method introduced in this work is to reduce the computational cost of CFD-CAA tool-chains for installation noise predictions of unconventional rotor configurations, at an acceptable level of accuracy. The test cases considered confirm the model capability of adequately predicting the different sound response of the configurations investigated. The BEMT-based model is seen to be noticeably influenced by non-negligible velocity fluctuations. Further validation with available experimental data will be considered in future contributions, investigating the effect of diffusion of vorticity in the generated sound response.

Acknowledgments

We would like to acknowledge the funding by the Deutsche Forschungsgemeinschaft (DFG, German Research Foundation) under Germany's Excellence Strategy –EXC 2163/1-Sustainable and Energy Efficient Aviation –Project-ID 390881007.

References

[1] Dunn, M., and Tinetti, A., "Advanced Time Domain Noise Prediction Methods for Open Rotors and Installation Effects," AIAA 2012-2217. 18th AIAA/CEAS Aeroacoustics Conference (33rd AIAA Aeroacoustics Conference). June 2012. https://doi.org/10.2514/6.2012-2217

[2] Drofelnik, J., Andrejasic, M., Mocan, B., Kosel, T., Christophe, J., Dominique, J. N., Schram, C. F., Hajczak, A., Stoica, C., Balasa, R., and Manea, M., "Measurement and modelling of aero-acoustic installation effects in tractor and pusher propeller architectures," AIAA 2021-2301. AIAA AVIATION 2021 FORUM. August 2021. https://doi.org/10.2514/6.2021-2301

[3] Nark, D. M., Jones, W. T., Buning, P. G., and Derlaga, J. M., "High-Lift Propeller Noise Prediction for a Distributed Electric Propulsion Flight Demonstrator," AIAA 2017-3713. 23rd AIAA/CEAS Aeroacoustics Conference. June 2017. https://doi.org/10.2514/6.2017-3713

[4] Brown, K., Fleming, J., Langford, M., Walton, W., Ng, W., Schwartz, K., Wisda, D., and Burdisso R., "Reduced-Order Prediction of Unsteady Propeller Loading and Noise from Pylon Wake Ingestion," AIAA Journal 2021 59:9, 3304-3316 https://doi.org/10.2514/1.J060109

[5] Guo, Y., and Thomas, R. H., "Experimental Study on Open Rotor Noise Shielding by Hybrid-Wing-Body Aircraft," AIAA Journal 2016 54:1, 242-253 https://doi.org/10.2514/1.J054243

[6] Dürrwächter, L., Keßler, M., and Krämer, E., "Numerical Assessment of Open-Rotor Noise Shielding with a Coupled Approach," AIAA Journal 2019 57:5, 1930-1940 https://doi.org/10.2514/1.J057531

[7] Smith, D. A., Filippone, A., and Barakos, G. N., "Noise Source Analysis in Counter-Rotating Open Rotors," AIAA Journal 0 0:0, 1-14 https://doi.org/10.2514/1.J060886

[8] Stuermer, A. W., "Validation of Installation Effect Predictions through Simulations of Contra-Rotating Open Rotors at Low-Speed Flight Conditions," AIAA 2015-2886. 33rd AIAA Applied Aerodynamics Conference. June 2015. https://doi.org/10.2514/6.2015-2886

[9] Winkler, J., Reimann, C. A., Reba, R., Ali, A. A., and Gumke, C., "Inlet and Aft Tonal Noise Predictions of a Full-Scale Turbofan Engine with Bifurcation and Inlet Distortion," AIAA 2017-3034. 23rd AIAA/CEAS Aeroacoustics Conference. June 2017. https://doi.org/10.2514/6.2017-3034

[10] Winkler, J., Reimann, C. A., Reba, R. A., and Gilson, J., "Turbofan Inlet Distortion Noise Prediction with a Hybrid CFD-CAA Approach," AIAA 2014-3102. 20th AIAA/CEAS Aeroacoustics Conference. June 2014. https://doi.org/10.2514/6.2014-3102

[11] Romani, G., Ye, Q., Avallone, F., Ragni, D., and Casalino, D., "Fan Noise Boundary-Layer Ingestion Installation Effects for NOVA Aircraft Configuration," AIAA 2019-2429. 25th AIAA/CEAS Aeroacoustics Conference. May 2019. https://doi.org/10.2514/6.2019-2429

[12] Mosson, A., Binet, D., and Caprile, J., "Simulation of the Installation Effects of the Aircraft Engine Rear Fan Noise with ACTRAN/DGM," AIAA 2014-3188. 20th AIAA/CEAS Aeroacoustics Conference. June 2014. https://doi.org/10.2514/6.2014-3188

[13] Franco, A., Ewert, R., Moessner, M., and Delfs, J. W., "Towards a Fast Non-Empiric Source Model for Installed Rotor Noise," AIAA 2021-2240. AIAA AVIATION 2021 FORUM. August 2021. https://doi.org/10.2514/6.2021-2240

[14] Samuelsson, I. (FFA): "Low speed propeller slipstream aerodynamic effects," Test Case Number E6 of "A Selection of Experimental Test Cases for the Validaton of CFD Codes," AGARD-AR-303, Vol. II.

[15] Raichle, A., “Flux Conservative Discretization of the Actuator Disk Model as a Discontinuity Surface,” Ph.D. thesis, Technical University Braunschweig, 2017.

[16] Gerhold T., "Overview of the Hybrid RANS Code TAU," In Kroll N., Fassbender J.K. (eds) MEGAFLOW - Numerical Flow Simulation for Aircraft Design, Notes on Numerical Fluid Mechanics and Multidisciplinary Design, vol 89. Springer, Berlin, Heidelberg, 2005. https://doi.org/10.1007/3-540-32382-1_5

[17] Spalart, P., and Allmaras, S., "A one-equation turbulence model for aerodynamic flows," AIAA 1992-439. 30th Aerospace Sciences Meeting and Exhibit. January 1992. https://doi.org/10.2514/6.1992-439